

# Characterization of Silicon Strip Sensors

Lukas Bertsch

lukas.bertsch@tu-dortmund.de

Tabea Hacheney

tabea.hacheney@tu-dortmund.de

Tom Troska

tom.troska@tu-dortmund.de

Date: 30th of April 2024

TU Dortmund University – Faculty of Physics

# Contents

<b>1</b>	<b>Motivation</b>	<b>3</b>
<b>2</b>	<b>Theory</b>	<b>3</b>
2.1	Semiconductors . . . . .	3
2.2	Doping of semiconductors . . . . .	4
2.3	The pn-junction . . . . .	4
2.4	Interaction of ionising radiation with matter . . . . .	5
2.4.1	The beta decay . . . . .	6
2.4.2	Interactions of electrons in matter . . . . .	7
2.5	Pedestals and Noise . . . . .	7
<b>3</b>	<b>Experimental setup and measurement process</b>	<b>9</b>
3.1	Detector unit . . . . .	9
3.2	Control unit . . . . .	10
3.3	Measuring tasks . . . . .	11
3.3.1	Current - voltage characteristic . . . . .	12
3.3.2	Pedestals and noise . . . . .	12
3.3.3	Calibration measurements . . . . .	12
3.3.4	Measuring characteristics of the strip sensors . . . . .	12
3.3.5	Charge Collection Efficiency . . . . .	13
3.3.6	Large source scan . . . . .	13
<b>4</b>	<b>Analysis</b>	<b>13</b>
4.1	Current - voltage characteristic . . . . .	13
4.2	Pedestals, noise and common mode shift . . . . .	13
4.3	Calibration measurements . . . . .	14
4.4	Characteristics of the strip sensor . . . . .	17
4.5	Charge collection efficiency . . . . .	19
4.5.1	CCEL . . . . .	19
4.5.2	CCEQ . . . . .	20
4.6	Large source scan . . . . .	20
<b>5</b>	<b>Discussion</b>	<b>23</b>
	<b>References</b>	<b>24</b>

# 1 Motivation

Semiconductor detectors play an important role in the detection of particles at experiments like ATLAS at the Large Hadron Collider (LHC) at CERN. In this experiment, the characteristics of a silicon strip sensor and its readout electronics are examined with a Educational Alibava System (EASy). Particle interactions stimulated by a laser and a strontium-90 source are measured and the data is processed and analysed.

## 2 Theory

Silicon strip sensors are semiconductor detectors which are used to measure particle tracks. For example, the *Inner Detector* (ID) at ATLAS is composited of the *Pixel Detector* in the innermost layers and the *Silicon Strip Detector* (SCT). When compared to higher resolution pixel sensors, silicon strip sensors offer a good trade off between spatial resolution and cost effectiveness. The working principle of such detectors is discussed in the following chapter.

### 2.1 Semiconductors

The conduction properties of a material are defined by their electron bands. The gap between the highest filled band (valence band) and the lowest unfilled band (conduction band) is called bandgap. Depending on the bandgap, materials are categorised as metals, semiconductors or insulators as shown in Figure 1. Metals are characterised by overlapping

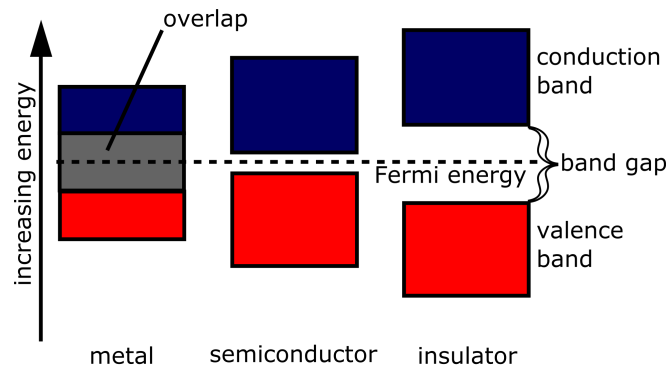


**Figure 1:** Electron bands for different types of materials [1].

conduction and valence bands and have no bandgap, therefore they are conductive. For insulators, the band gap is around 4 eV or higher, which is why they are not conductive because the energy from thermal excitation is much smaller ( $\approx 30$  meV). Semiconductors typically have a bandgap of 1 to 5 eV and are also not conductive at  $T = 0$  K. However, at roomtemperature electrons can be excited to the conduction band. The ‘hole’ that they leave behind can be viewed as a quasiparticle that carries a positive charge and has an effective mass. Silicon, which is used for the detector in this experiment, has a

bandgap of 1.107 eV and an intrinsic charge carrier density of  $1.5 \times 10^{10} \text{ cm}^{-3}$ . Silicon belongs to the *element semiconductors*, other types are *compound semiconductor* like gallium arsenide or *organic semiconductors* which consist of carbon compounds.

## 2.2 Doping of semiconductors

The intrinsic charge carrier density for pure (= intrinsic) semiconductors is often too small to effectively use them. Therefore, atoms with a different amount of valence electrons are introduced into the crystal structure of a semiconductor to increase its conductivity. This process is called doping. Silicon has 4 valence electrons and forms a diamond lattice structure. Silicon doped with pentavalent atoms, such as arsenic, is called a *n-type* semiconductor. The fifth valence electron is not needed in the crystal bond and acts as a free charge carrier on a new level in the band diagram right below the conduction band which is called *donator level*. This effectively reduces the band gap. Electrons in the donator level can easily be excited to the conduction band which increases conductivity. Alternatively, trivalent atoms, like boron, can be used. The semiconductor is then called *p-type*. The missing electron in the bond can be seen as a hole, that can move freely in the coulomb potential of the crystal lattice. A new level, called *acceptor level*, arises in the band diagram right above the valence band. Electrons from the valence band can be excited to the acceptor level. The two types of doping are visualised in Figure 2.

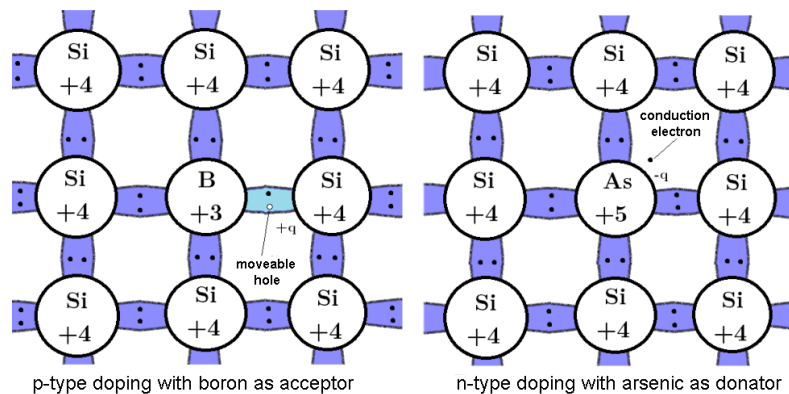


**Figure 2:** Schematic representation of an n- and p-type doped silicon semiconductor (Adapted from [4]).

## 2.3 The pn-junction

By connecting a n-type to a p-type semiconductor, a diode can be created. At the transition between the n- and p-type semiconductors (the *pn-junction*) electrons from the n-side and holes from the p-side diffuse towards the respective other side and recombine. Because of the recombination, no free charge carriers remain at the junction. The stationary doping atoms are now missing an electron or hole and cause a positive charge at the n-side and a negative charge at the p-side, resulting in an electric field. Through

the electric field, the remaining charge carriers drift in the opposite direction. When equilibrium is reached between drift and diffusion, a zone around the pn-junction with no charge carriers is created - the *depletion zone*. The difference in the potential of the two sides is called diffusion voltage  $U_D$ . By applying an external electric field (bias voltage), this effect is either weakened (+ on p-side, - on n-side) and a light emitting diode is created, or the effect is amplified (+ on n-side, - on p-side) which increases the thickness of the depletion zone. This is the case for the detector operation of the diode. Electron-hole pairs created in the depletion zone (e.g. by a traversing particle) are drawn to the p- and n-side which generates a measurable current. The thickness of the depletion zone depends on the applied voltage and can be calculated as

$$d(U) = \sqrt{\frac{2\varepsilon(U_D + U)}{qN_{\text{eff}}}}, \quad (1)$$

where  $\varepsilon$  is the dielectric constant of the material and  $N_{\text{eff}}$  is the effective charge carrier density of the crystal. It is given by

$$N_{\text{eff}} = \frac{N_D N_A}{N_D + N_A}, \quad (2)$$

where  $N_D$  and  $N_A$  are the doping concentrations of the donors and acceptors, respectively. For the detector operation, the whole crystal should be depleted, requiring a minimum depletion voltage of  $U_{\text{dep}}$ . Using Equation 1 and neglecting the diffusion voltage  $U_D$ ,  $U_{\text{dep}}$  can be calculated via

$$U_{\text{dep}} \approx \frac{q}{2\varepsilon} N_{\text{eff}} D^2. \quad (3)$$

Here,  $D$  is the thickness of the sensor. With  $U_{\text{dep}}$  given, the thickness  $d_c$  of the depletion zone can be approximated via

$$d_c(U) = \begin{cases} D\sqrt{U/U_{\text{dep}}} & , U < U_{\text{dep}} \\ D & , U \geq U_{\text{dep}}. \end{cases} \quad (4)$$

Ideally, only energy deposition of ionising particles causes a current. In reality however, electron-hole pairs are also created by thermal excitation and are drawn to the poles, causing a *leakage current*. The leakage current increases with the bias voltage. In Figure 3, a measured leakage current for the system used here, is plotted against the bias voltage. As can be seen from the plot, the leakage current strongly increases, until the depletion voltage  $U_{\text{dep}}$  is reached and then continues to increase linearly. From this measurement, the depletion voltage can be obtained.

## 2.4 Interaction of ionising radiation with matter

In this experiment, the EASy detector system is employed to measure ionising particles from a strontium-90 source. Therefore, it is important to understand the energy deposition of ionising particles in matter.

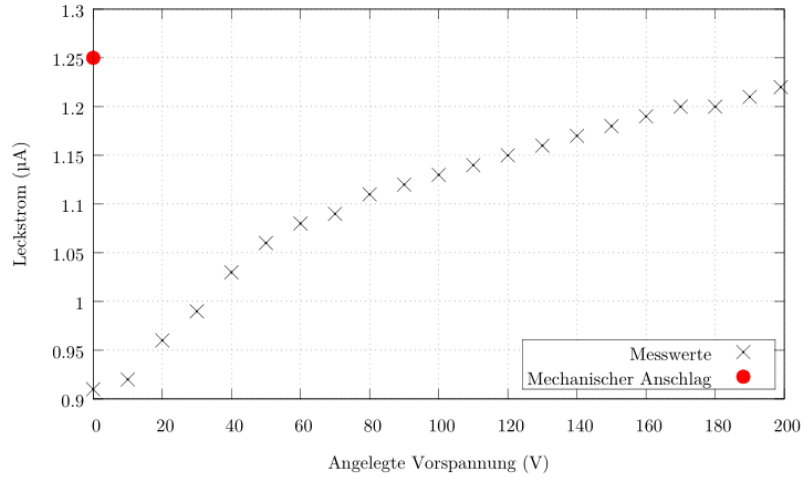


**Figure 3:** Measurement of the leakage current against the bias voltage for the Educational Alibava system used in this experiment [4]. The depletion voltage can be read from the plot as 60 V.

#### 2.4.1 The beta decay

In general, the beta decay proceeds over

$$n \rightarrow p + e^- + \bar{\nu}_e.$$

The free binding energy is randomly distributed to the decay products (i.e. the electron and neutrino), resulting in an energy spectrum of the electron as shown in Figure 4. As

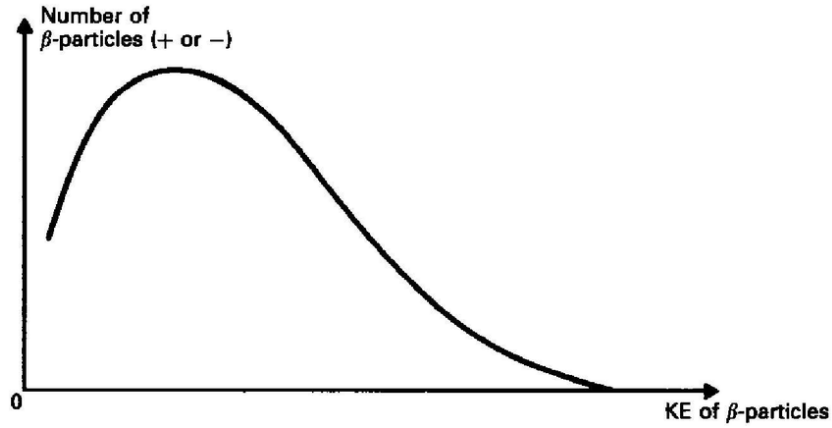
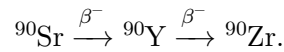


**Figure 4:** Electron energy spectrum of a  $\beta^-$  decay [2].

can be seen in the plot, a material dependent maximum energy can be reached. The decay chain of strontium-90 is



The strontium has a half-life of 28.78 a while yttrium has a half-life of 59 d and the zirconium is stable. Both  $^{90}\text{Sr}$  and  $^{90}\text{Y}$  decay via the  $\beta^-$  decay. The maximum kinetic energy of the electron is 0.546 MeV and 2.28 MeV for strontium and yttrium, respectively [3]. For a simple 1-step decay chain, the activity (decays per time) is given by

$$A(t) = -\frac{dN}{dt} = \lambda N_0 e^{-\lambda t},$$

with the initial number of atoms  $N_0$  and the decay constant  $\lambda$  of the atom. The unit is Bq = s $^{-1}$ . For a decay chain, this is more complicated, but in the limit  $T_{1/2,^{90}\text{Sr}} \gg T_{1/2,^{90}\text{Y}}$  the total activity is effectively the  $^{90}\text{Sr}$  activity doubled.

### 2.4.2 Interactions of electrons in matter

When traversing a material, the electrons interact with the nucleus and electrons of the atomic shell and deposit energy. Since the kinetic energy of the electrons in this experiment is not large enough, bremsstrahlung, inelastic collisions with the nuclei and Cherenkov radiation are not considered. The relevant effect here, is the ionisation of the atoms by collisions of the incoming electrons with shell electrons. The average energy loss per distance of the electron is given by the modified Bethe-Bloch equation [3]

$$-\frac{dE}{dx} = 2N_A m_e c \rho \frac{Z}{A} \frac{1}{\beta^2} \left[ \ln \left( \frac{\tau^2(\tau+2)}{2(I/m_e c^2)^2} \right) + F(\tau) - \delta - 2\frac{C}{Z} \right]. \quad (5)$$

Here,  $Z$  and  $A$  are the proton- and mass number of the material,  $\rho$  the materials density,  $m_e$  is the electron mass,  $c$  the speed of light,  $\beta$  the relativistic beta factor,  $N_A$  the Avogadro constant and  $\delta$  and  $C$  the density and envelope corrections.  $I$  is the average excitation potential and  $\tau = 1 - \gamma$  corresponds to the kinetic energy of the electron.  $F(\tau)$  is determined as

$$F(\tau) = 1 - \beta^2 + \frac{\frac{\tau^2}{8} - (2r_e + 1)\ln(2)}{(\tau + 1)^2}$$

with  $r_e$  the classic electron radius. For  $^{90}\text{Sr}$  it follows, that an electron of maximum energy deposits an energy of 3.88 MeV/cm in pure silicon [4].

In this experiment, the spectrum of energy deposition of the electrons in the silicon can best be described by a convolution of a Gaussian- and a Landau- distribution as shown in Figure 5.

## 2.5 Pedestals and Noise

In this experiment, the charge deposition is given in counts of the analogue-to-digital converter (ADC counts) and therefore has to be converted to keV on the basis of a calibration measurement. The calibration generates a specified amount of electron-hole pairs which are then converted into ADC counts. To create one electron-hole pair in silicon, an energy of 3.6 eV [4] is required.

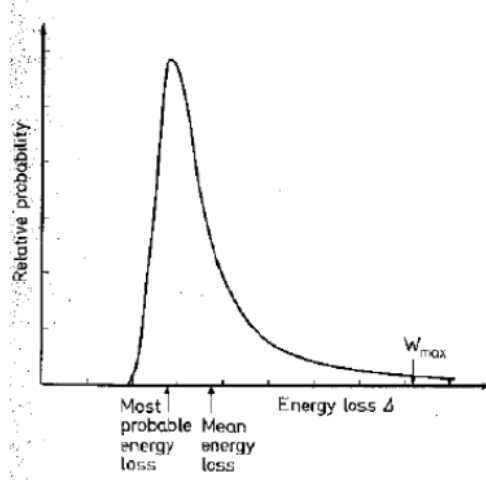


**Figure 5:** Energy deposition of electrons in a 300  $\mu\text{m}$  silicon sensor [4].

When measuring, the ADC counts always include noise. In order to get the signal count, all unwanted effects have to be subtracted. In total, the measured ADC counts for a signal  $k$  at strip  $i$  is given by

$$\text{ADC}(i, k) = P(i, k) + D(i, k) + \text{Signal}(i, k) + \text{Noise}(i, k). \quad (6)$$

The *pedestal*  $P(i, k)$  is the mean value of ADC counts for a strip without external signal and can be calculated via

$$P(i) = \frac{1}{N} \sum_{k=1}^N \text{ADC}(i, k) \quad (7)$$

from  $N$  measurements without signal.  $D(k)$  is called the *Common Mode Shift* or *Common Noise* and describes a global disturbance affecting all strips during an event and can be determined as

$$D(k) = \frac{1}{128} \sum_{i=1}^{128} (\text{ADC}(i, k) - P(i)). \quad (8)$$

The common noise is gaussian distributed around 0. Finally, the noise of each strip can be calculated using the root-mean-square of the ADC counts after subtracted pedestals and common noise:

$$\text{Noise}(i) = \sqrt{\frac{1}{N-1} \sum_{k=1}^N (\text{ADC}(i, k) - P(i) - D(k))^2}. \quad (9)$$

When measuring a true signal, this calculation has to be performed a second time, where signals several standard deviations above the noise level are then sorted out.



### 3 Experimental setup and measurement process

For the experimental setup, the Alibava EASy detector system is used. It consists of a control unit, a detector unit and a computer to control the different measuring modes and for interpreting the taken data. This is done with the Alibava Graphical User Interface (GUI). The detector and control unit are connected via a ribbon cable, while the control unit and the computer are connected via USB. In some measuring tasks, an additional optical fiber cable is used. In the source measurements, a radioactive source and a LEMO cable for the built-in diode are needed.

#### 3.1 Detector unit

The detector unit consists of the semiconductor sensor and readout electronics. A laser system is put on top of the detector unit, to excite the sensor and trigger signals. The laser system can be put into two different positions. The "L" position is used for laser measurements and the "Q" position is used for a source measurement with radioactive material. Triggered signals in the sensor are amplified in the BEETLE chip and converted into a voltage signal, which can later be interpreted by the control unit. The signal is kept in a pipeline by the BEETLE chip, until there is an incoming triggering signal from the control unit. Only then will the recorded signal be passed on to the control unit and computer. If there is no trigger signal, the data is discarded.

The depletion voltage of the used semiconductor is usually about  $60 - 70 \text{ V}$  [4]. It can be controlled and adjusted via a knob on the control unit. Knowing the exact depletion voltage will be one of the first measuring tasks, such that the following tasks can be carried out using the highest efficiency possible. The detector unit can be seen in Figure 6.

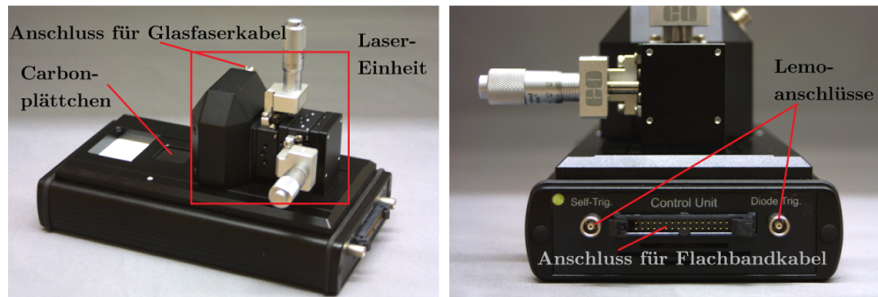


**Figure 6:** The detector unit in "Q" position. Top view (left) and side view (right) [4].

The used semiconductor sensor consists of a  $300 \mu\text{m}$  thick n-doped silicon layer which is covered by metallisation on one side. Ohmic resistors are used as a power supply for the sensor. The other side of the silicon layer is covered by 128 p-doped implants. This creates a pn-semiconductor. The p-doped strip sensors are insulated from each other, so no current can flow directly between them. This enables a localisation of the incoming signal by reading out which channel got excited. The strips are then covered by a silicon oxide layer to prevent leakage current to be detected in the readout electronics.

A top-down view and a detailed schematic of the sensor is shown in Figure 7. The guard ring blocks charge to flow uncontrolled beyond the sensor and the bias ring supplies the semiconductor with a bias voltage to enlarge the depletion zone. Due to the p-implants being embedded in the n-base, the semiconductor is called an p-in-n sensor.

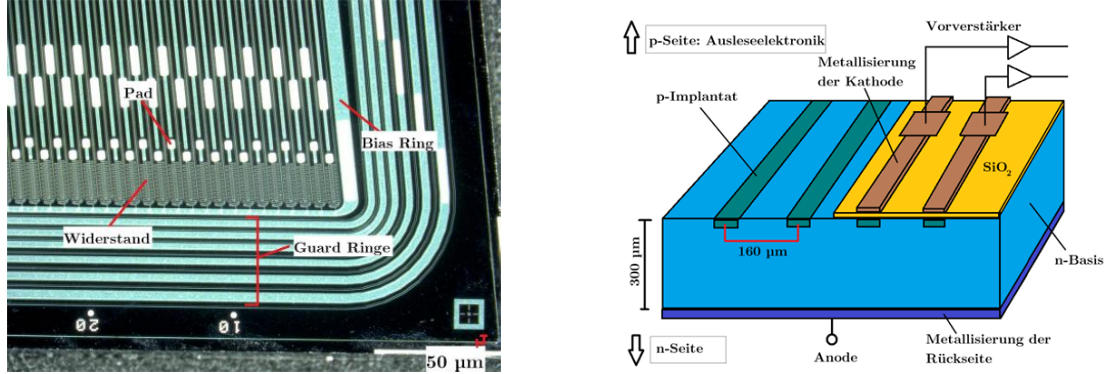


**Figure 7:** Macroscopic top down view (left) and a schematic view of the construction of the whole sensor (right) [4].

The electrons and holes in the n- and p-doped layer recombine if the applied bias voltage is not high enough. If the bias voltage is applied, an electric field is created such that electrons and holes are separated. A depletion zone is caused and gets bigger for higher applied bias voltage. The quality of the sensor can be defined by the charge collection efficiency (CCE). The higher the applied bias voltage, the bigger the depletion zone and the greater the CCE gets until a maximum is reached at  $U_{\text{dep}}$ . This is when the sensor is fully depleted. The CCE can be calculated for the applied voltage as

$$\text{CCE}(U) = \frac{1 - \exp\left(\frac{-d_c(U)}{a}\right)}{1 - \exp\left(\frac{-D}{a}\right)}. \quad (10)$$

$D$  is the thickness of the sensor,  $d_c$  is the thickness of the depletion zone and  $a$  is the mean penetration depth of the laser into the silicon. The used sensor has a thickness of  $D = 300 \mu\text{m}$ . For the source measurement and therefore the excitation with electrons, the CCE is proportional to  $d_c$ .

The used laser is supplied with energy and controlled via the control unit. A fiber cable transfers the 5 ns long laser pulses from the control unit to the detector unit. The platform has to be in the "L" position for those measurements. It has a wavelength of 980 nm, a diameter of 20 μm and a peak power of 0.6 mW.

The horizontal and vertical position of the laser output into the sensor can be adjusted with micrometer screws with an accuracy of 10 μm [4].

### 3.2 Control unit

The control unit is used for controlling the laser and the bias voltage of the sensor. It also interprets the taken data into ADC Counts which can be recorded with the computer.

The leakage current is measured with an amperemeter of the control unit. It can be read out with an accuracy of  $0.01 \mu\text{m}$  [4].

As explained in subsection 2.5, a lot of noise by the source measurement is also recorded and converted into ADC counts by the detector and control unit. To distinguish between background and relevant data, a signal-to-noise cut is applied to the data. This signal-to-noise ratio can be chosen freely and is set as 5 here. If the signal is five times higher than the noise, it is considered for the analysis. Otherwise it is discarded.

Another source of noise is also the triggering of multiple sensors by only one real signal. This happens, when a particle passes near the edge of a strip. The created voltage can cause other strips to fire as well. Another effect would be crosstalk, where a particle crosses perpendicular to the surface and therefore through multiple strips.

### 3.3 Measuring tasks

The measuring tasks in 3.3.4 and 3.3.5 use the laser. For these tasks, the fibre optic cable needs to be plugged into the detector unit and the control unit and the pedestal needs to be in the "L" position.

For the measurements in 3.3.5 and 3.3.6 the source is used. For this, the detector unit needs to be put into the box with the source. The detection unit is additionally covered with lead bricks, to prevent radiation to come out of the experimental setup. It is still advised not to directly stand over or under the source, since there is no lead protection. The pedestal needs to be put into the "Q" position and an additional LEMO cable must be plugged into the diode trigger of the detector unit and into the control unit. The carbon plate with the source needs to be directly on top of the sensor. The used setup for the source measurements and the process is shown in Figure 8.

For the source measurements, an additional diode is used, which is placed a few millimetres below the sensor. It ensures, that only those electrons are regarded, that also triggered a signal in the diode. Only those electrons with enough energy can excite electron-hole pairs in the sensor and additionally the diode. If the diode triggers a signal, the BEETLE chip switches off and the signal gets transferred to the control unit.

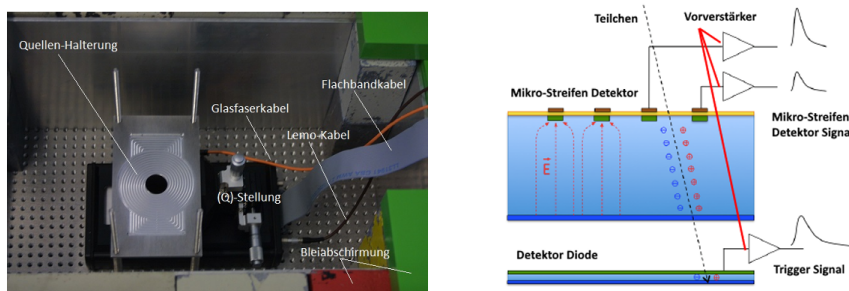


**Figure 8:** Experimental setup for the measurements using the radioactive source (left) and a schematic view of how the sensor is triggered with the additional diode (right) [4].

### **3.3.1 Current - voltage characteristic**

The current-voltage characteristic is measured by adjusting the bias voltage in 10 V steps. This way, the depletion voltage can be extracted. The bias voltage of 0 V must be carefully set from a higher voltage, since rotating the knob for the bias to the lowest possible voltage actually applies a voltage in forward direction which causes the semiconductor to conduct.

Use a bias voltage at least 20 V higher than the estimated depletion voltage for the following measurements.

### **3.3.2 Pedestals and noise**

For this measurement, the underlying pedestal is to be measured. To do this, the "Pedestal Run" is chosen in the computer interface and a run for 1000 events is started. The pedestal and noise for each strip should be plotted and the values of the common mode represented graphically.

### **3.3.3 Calibration measurements**

First, the optimal delay has to be determined. For this, the control unit sends a defined delayed electron pulse to the BEETLE chip, via the ribbon cable. This is needed to convert the recorded ADC counts into charge and to interpret the data in the following tasks. The BEETLE chip transmits the measured ADC counts to the control unit. The ADC counts are then plotted against the used charge. Like this, a calibration curve is obtained which can be used to convert the ADC counts of the following tasks into charge. To do this, first, a "Delay Measurement" is started. This measures the amount of data obtained for different delays between the signal and the readout of the signal. The peak of the obtained data series is the best possible delay and is used for the following measurements.

With the optimal delay applied, calibration measurements for five different channels are started. For a single channel, an additional measurement for a bias voltage of 0 V is done. The dependence between the ADC and the charge is to be plotted. The measurement at 0 V is compared to the other ones above the depletion voltage.

### **3.3.4 Measuring characteristics of the strip sensors**

In this task, the structure of the sensor strips is to be observed. First, the optimal delay between the laser and the BEETLE chip is measured by using the "Laser Sync." option in the GUI. With the optimal delay applied, 35 measurements with each 1000 recorded events are carried out. Each measuring point should cover an interval of 10  $\mu\text{m}$ . The signal of relevant strips is to be plotted as a function of the laser position. The extension of the laser is to be determined and the number of strips is to be noted.

### 3.3.5 Charge Collection Efficiency

The CCE is measured for both the laser and the source. Since the last measurement included the laser, this setup is used first. The bias voltage should be increased from 0 V to 200 V in 10 V steps and at least 1000 events should be recorded for each measuring step. The efficiency of the detector is to be determined as a function of the bias voltage and the penetration depth of the laser  $a$  is to be determined.

For the measurement with the source, the detector unit is to be put into the setup for the source measurement and the platform put into the "Q" position. Again, the bias voltage is increased from 0 V to 200 V in 10 V steps and at least 10 000 events should be recorded for each measuring step. The mean cluster energy is to be plotted as a function of the bias voltage and the results compared to the laser measurement.

### 3.3.6 Large source scan

For the final measurement, the source is to be examined. For this, a RS Run for 1 000 000 events is to be performed. The data is to be presented graphically in a meaningful way and the number of events per channel should be displayed. The energy spectrum should be shown in ADC and keV as well. With that, the mean value of the deposited energy and the MPV is to be determined and the result evaluated.

## 4 Analysis

This section focuses on the analysis of the measured data. Because of a malfunctioning cable connection, many of the tasks could not be completed and for those that data could be taken, the trustworthiness can be questioned. The data for all of the tasks, except for the measurement of the current-voltage characteristic, were kindly provided by our supervisor.

### 4.1 Current - voltage characteristic

In a first step, the sensor current  $I$  is measured as a function of the applied bias voltage  $U$ . The resulting data are shown in Figure 9. By comparing this plot with the theoretical prediction Figure 3, the depletion voltage  $U_{\text{dep}}$  is determined by identifying a kink in the graph. In the case of this data, this is particularly difficult. Reasons for this are further addressed in section 5. The depletion voltage estimated from the characteristic is  $U_{\text{dep}} = 60 \text{ V}$ .

In the following, a bias voltage of 80 V is used to ensure that the detector is depleted entirely.

### 4.2 Pedestals, noise and common mode shift

Like all electronic devices, silicon strip detectors are prone to electronic noise. Following Equation 6, the ADC counts consist not only of the signal but also the pedestal  $P(i, k)$ , the common mode shift  $D(k)$  and the noise  $N(i)$ . For the determination of these quantities,

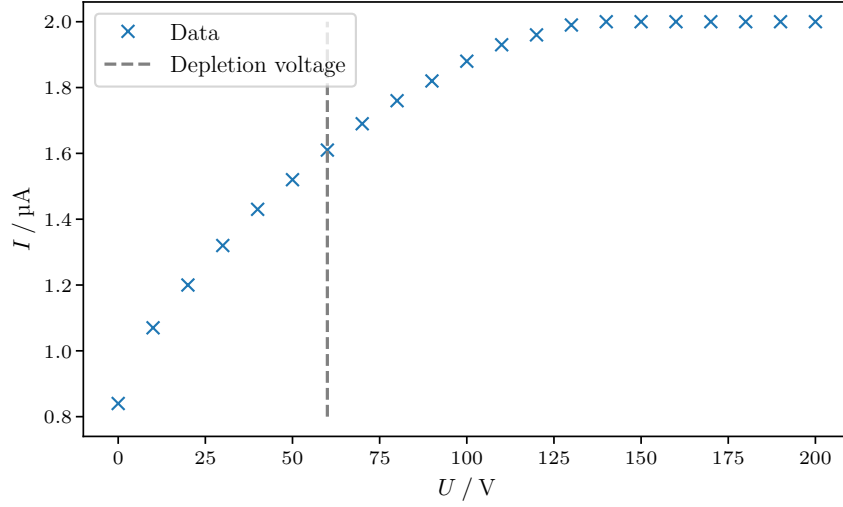


**Figure 9:** Plot of the measured current  $I$  dependent on the applied voltage  $U$ . The depletion voltage  $U_{\text{dep}} = 60 \text{ V}$  is shown as the dashed line.

the ADC counts for the strips are measured and used to calculate the target values. The counts of each individual strip without external signal is called the pedestal  $P(i, k)$  and is calculated via Equation 7. A graphic representation is given in Figure 10a. A global disturbance to all of the strips is referred to as the common mode shift  $D(k)$  and determined by averaging over the difference of the ADC counts and the pedestals (see Equation 8). This is visualized in Figure 10b. Taking the root-mean-square of the ADC counts subtracted of the pedestal and common mode shift yields the noise  $N(i)$  of each pixel. With the help of Equation 9, the data are represented in Figure 10c. Analyzing the common mode shift  $D(k)$  in Figure 10b, it is clear that the data follow a Gaussian distribution. For the noise  $N(i)$ , a uniform distribution with increasing noise at the sensors' edges is present.

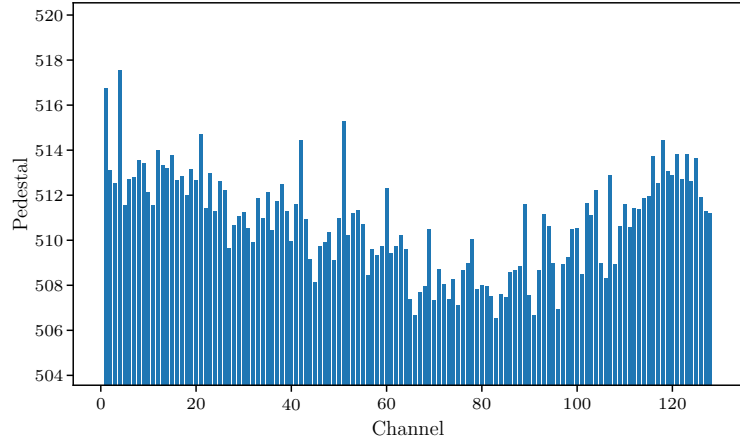
### 4.3 Calibration measurements

A proper calibration of the system is necessary to ensure a good quality of the data. Therefore, the delay time is optimized by performing a delay scan and determining the maximum value and entering this value into the GUI of the program.<sup>1</sup>

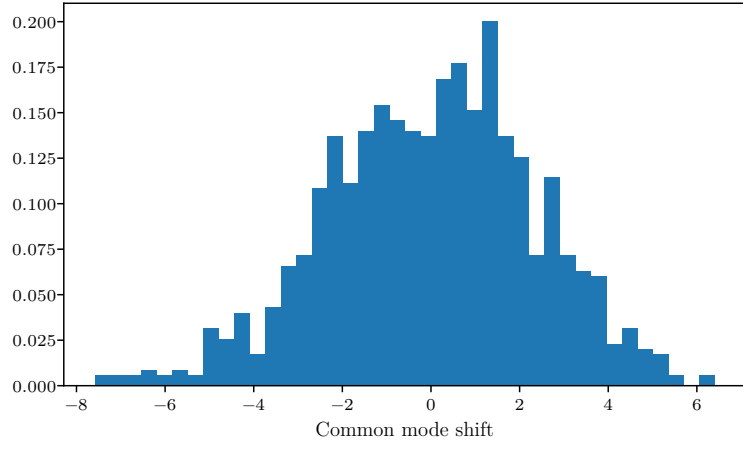
Moreover, a calibration run for five different channels is carried out. For this, a known charge is injected and the ADC counts are measured. Additionally, one calibration run for a bias voltage of  $U_{\text{bias}} = 0 \text{ V}$  is executed. In the diagrams of Figure 11, the calibration runs are depicted.

The measurements of the five different channels are mostly in agreement with each other while the  $U_{\text{bias}} = 0 \text{ V}$  run shows slightly less ADC counts.

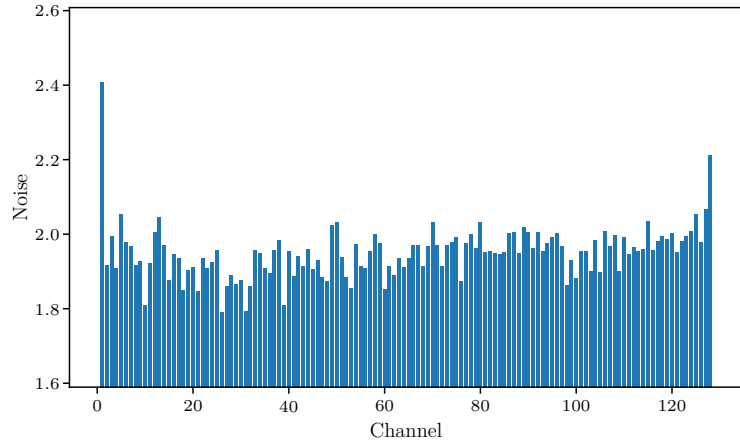
<sup>1</sup>The data to this are unfortunately lost because of the complications we had with the setup. A similar calibration is performed for the laser synchronization run in subsection 4.4.



(a) Pedestal  $P(i, k)$ .

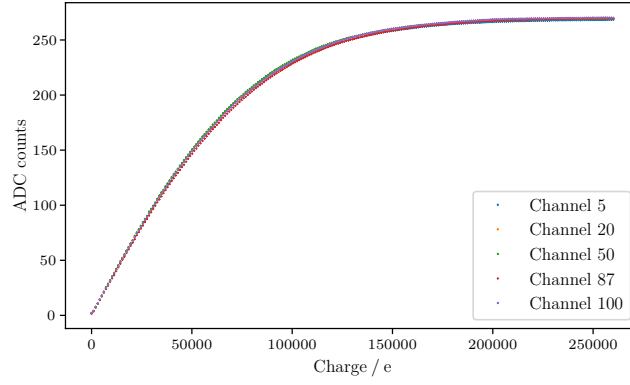


(b) Common mode shift  $D(k)$ .

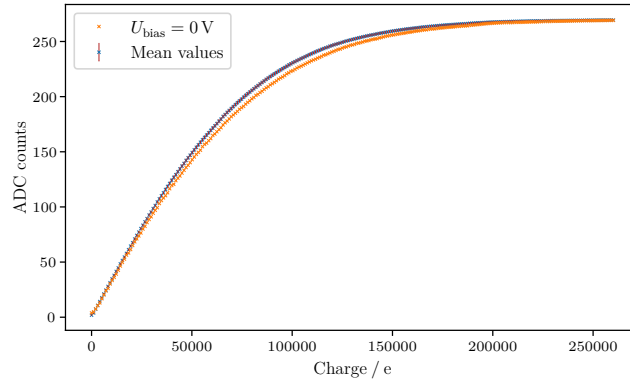


(c) Noise  $N(i)$ .

**Figure 10:** Visualization representation of the pedestal  $P(i, k)$ , common mode shift  $D(k)$  and noise  $N(i)$ .



(a) Individual channels



(b) Mean values and  $U_{\text{bias}} = 0 \text{ V}$ .

**Figure 11:** Calibration run: dependence of the ADC counts on the injected charge.



In addition to these plots, the injected charge is also plotted against the measured ADC counts and fitted with a fourth-degree polynomial function. This is performed in Figure 12. With the help of the python extension `scipy` [5], the parameters for a

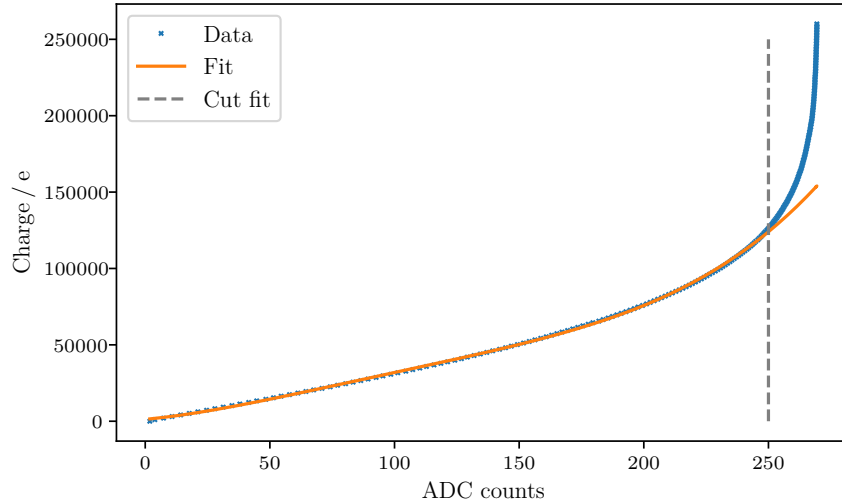


**Figure 12:** Plot of the injected charge and corresponding ADC counts. A fourth degree polynomial function is fitted to the data.

polynomial of the form  $f(x) = a + bx + cx^2 + dx^3 + ex^4$  are extracted as

$$\begin{aligned} a &= (1.2 \pm 0.4) \times 10^3 \frac{1}{e^0} \\ b &= (151 \pm 19) \frac{1}{e} \\ c &= (3.28 \pm 0.29) \frac{1}{e^2} \\ d &= (-0.0235 \pm 0.0017) \frac{1}{e^3} \\ e &= (6.34 \pm 0.32) \times 10^5 \frac{1}{e^4}. \end{aligned}$$

Later in subsection 4.6, this function is used to convert the ADC counts to a corresponding energy.

#### 4.4 Characteristics of the strip sensor

Among other variables, the pitch and the width of the strips are of high interest. These characteristics can be determined by exciting the sensor with a laser. Before these measurements can be conducted, the delay between the laser signal and the chip readout needs to be optimized. For that reason, a laser synchronization run is performed where

the delay time is varied and the ADC counts are measured. Such a run is shown in Figure 13. The delay time at which the ADC counts are maximized is evaluated as 64 ns and entered into the GUI of the program.

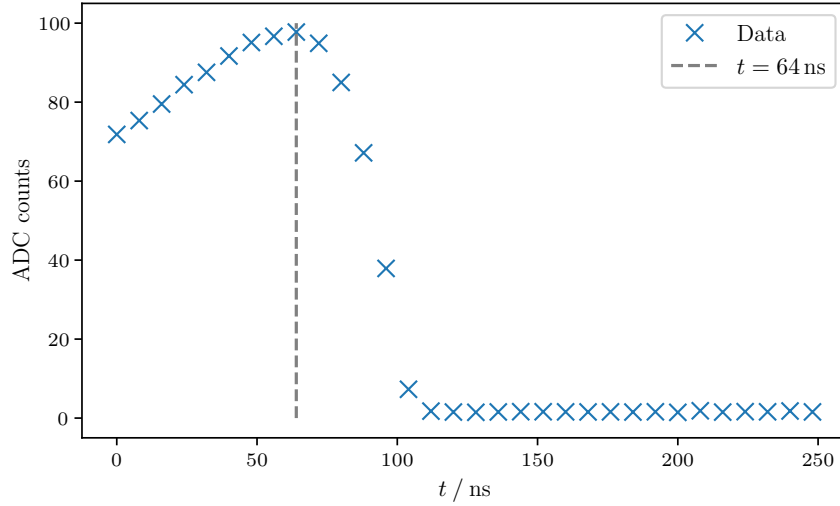


**Figure 13:** Graphical representation of the laser synchronization run with the ADC counts depending on the delay time  $t$ .

With the laser synchronized to the chip readout, the actual measurements of the strip sensor characteristics can begin. Therefore, the laser is moved in 10  $\mu\text{m}$  intervals along the sensor. The ADC counts are measured and represented graphically in Figure 14.

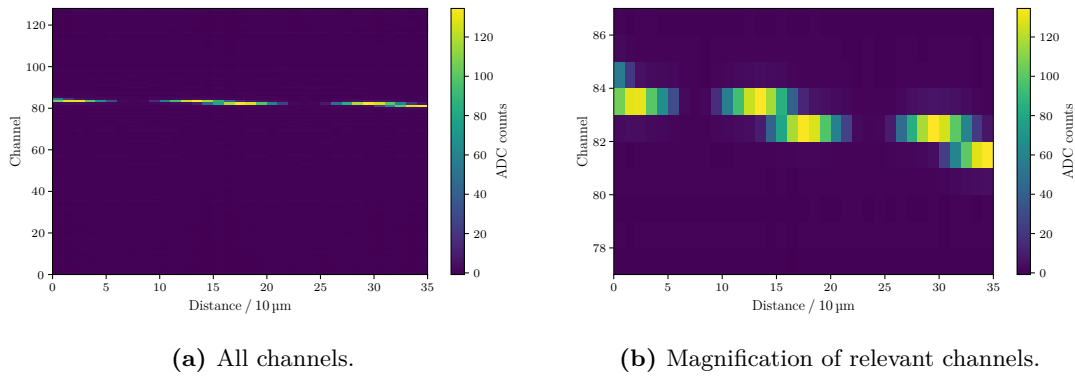


**Figure 14:** Laser scan: the ADC counts are depicted for each channel and distance along the axis where the laser is moved.

It is clear that the laser is focused on the strips with the channels 83 and 84. The ADC counts of these channels are further considered for the determination of the chips' characteristics (see Figure 15). The pitch of the sensor can be measured by calculating

the distance between the maxima of the ADC counts. The width of the strips follows from the width of the peaks.

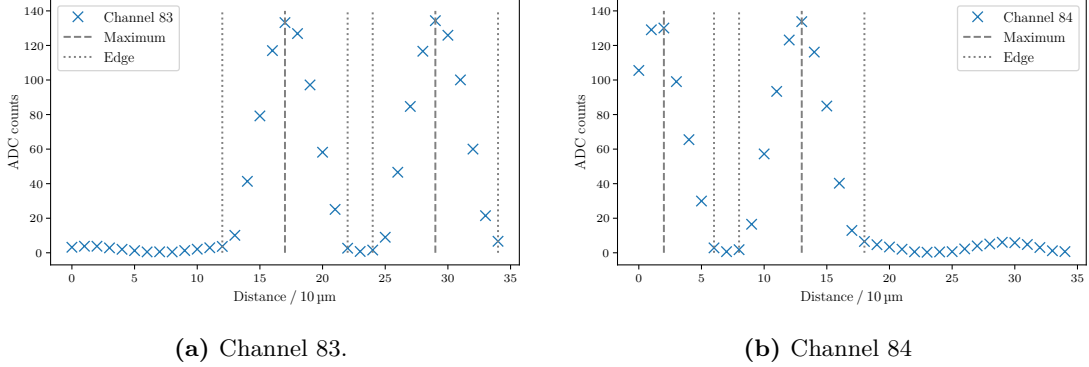


**Figure 15:** Depiction of the ADC counts and distance of the laser for the relevant channels 83 and 84.

**Table 1:** Results for the measurements of the pitch and strip width extracted from Figure 15. All values in  $\mu\text{m}$ .

	Start 1	End 1	Width	Start 2	End 2	Width	Max 1	Max 2	Pitch
Channel 83	120	220	100	240	240	100	170	290	120
Channel 84	-	60	-	80	180	100	20	130	110

## 4.5 Charge collection efficiency

In this part of the analysis, the charge collection efficiency (CCE) is determined in two manners. First, the laser is used to excite the sensor where a  $\beta^-$  source is employed later.

### 4.5.1 CCEL

With the help of a laser, that is sharply focused on one strip of the sensor, the CCE can be deliberated. Again, the ADC counts are recorded but this time the bias voltage is varied. Similar to the laser scan, the results are shown in a colormap, see Figure 16.

The penetration depth of the laser can be reconstructed by fitting Equation 10 to data of the relevant channel from Figure 16. Therefore, the ADC counts need to be normalized to their maximum. In theory, the ADC counts reach a plateau for values of the bias voltage greater than the depletion voltage. Because of imperfections, the measured plateau is not strictly constant. As a solution to this, the values are normalized to the mean value of the plateau.

The free parameter  $a$  from Equation 10 is identified as the penetration depth and determined as

$$a = (212 \pm 24) \mu\text{m}.$$

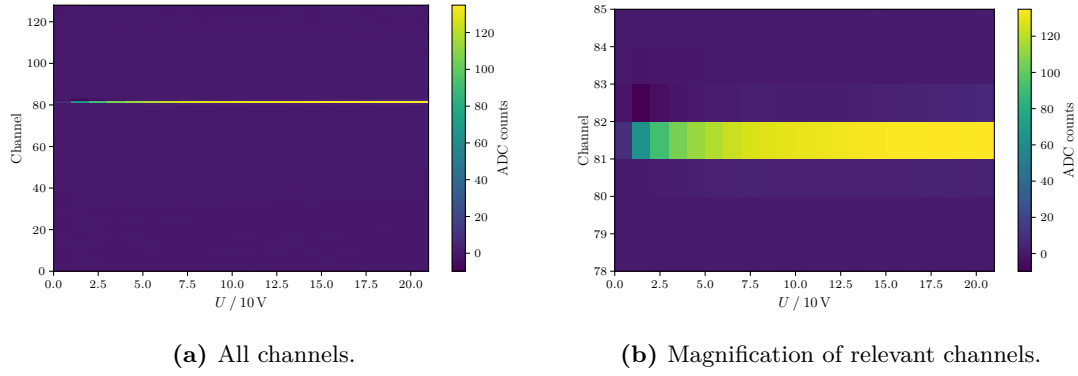


**Figure 16:** CCE laser scan: the ADC counts are depicted for each channel and applied bias voltage.

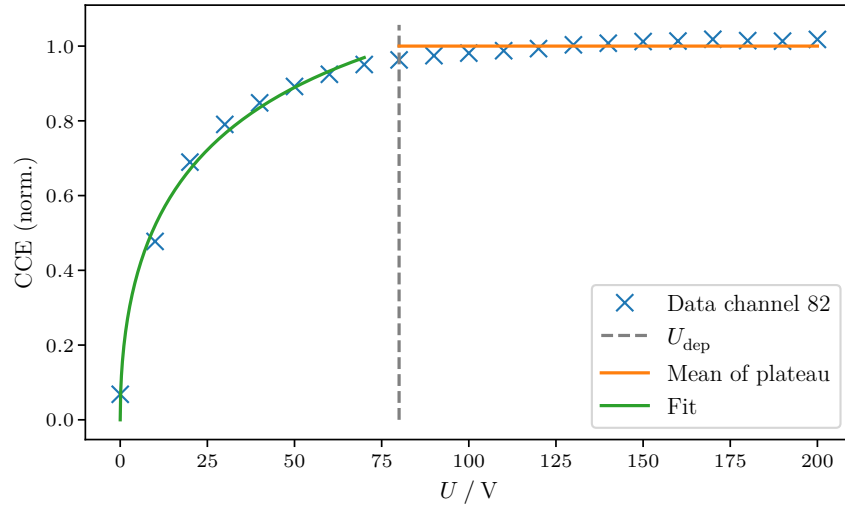


**Figure 17:** Laser CCE scan: normalized ADC counts for different bias voltages.

#### 4.5.2 CCEQ

Analogous to the previous analysis step, the measurement of the CCE with a  $\beta^-$  source yields a plot of the ADC counts in dependence of the bias voltage. This plot, represented in Figure 17 is similar to the laser CCE scan (Figure 17). For bias voltages greater than the depletion voltage of  $U_{\text{dep}} = 80 \text{ V}$  the ADC counts are mostly constant.

#### 4.6 Large source scan

In the final part of the measurement series, the sensor is exposed to the source for a total of approximately 1 000 000 events. In Figure 19, the data for this large source scan

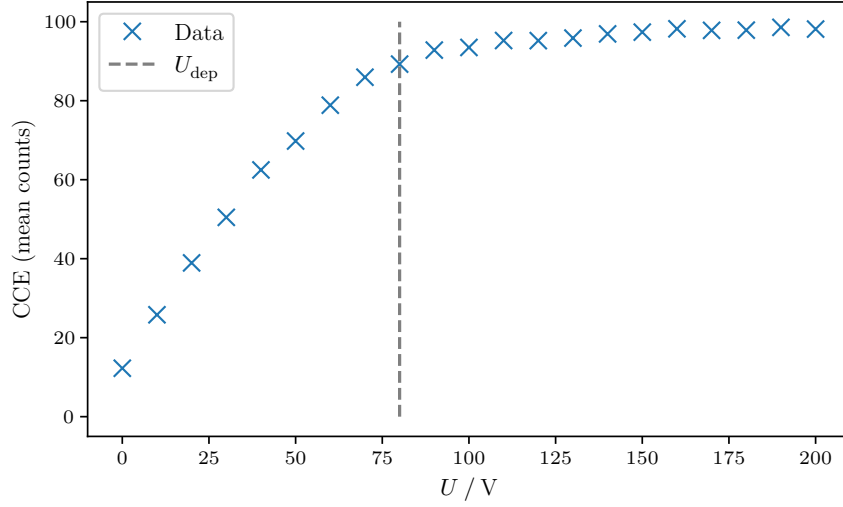


**Figure 18:** Source CCE scan: ADC counts for different bias voltages.

are represented. Figure 19a shows the number of clusters that each event caused. The number of responding channels to each cluster is depicted in Figure 19b. Here, no more than five different channels were triggered. The distribution of all the counts on all the channels is given in Figure 19c. The shape of the distribution suggests that the source was focused at the strips corresponding to the channels 70 to 90.

When binning the ADC counts for this large source scan, a maximum can be determined. With the help of the previously calculated correlation function of the ADC counts and charge (see subsection 4.3), the energy spectrum can be extracted. Therefore, the charge needed to create electron-hole pairs of 3.6 eV needs to be accounted for. The resulting distribution is displayed in Figure 20b.

The mean value of the energy as well as the most probable value are read off as

$$E_{\text{mean}} = 135.94 \text{ keV}$$

$$E_{\text{MPV}} = 89 \text{ keV}.$$

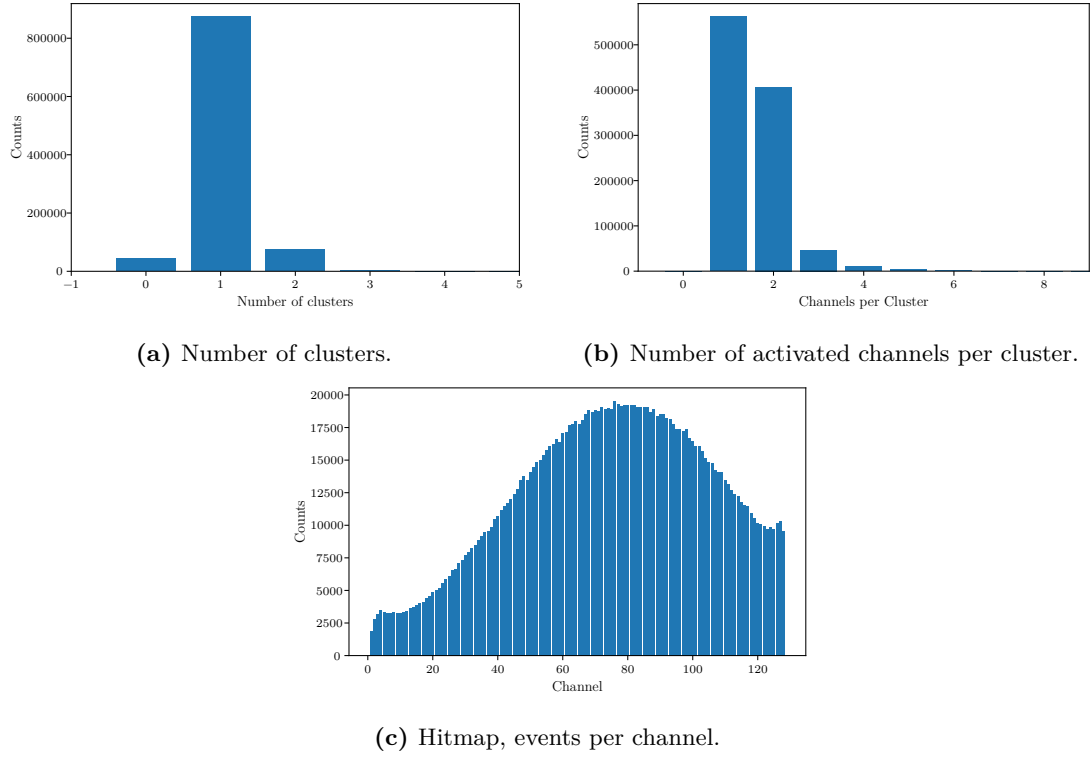


**Figure 19:** Visualization of different aspects of the large source scan.

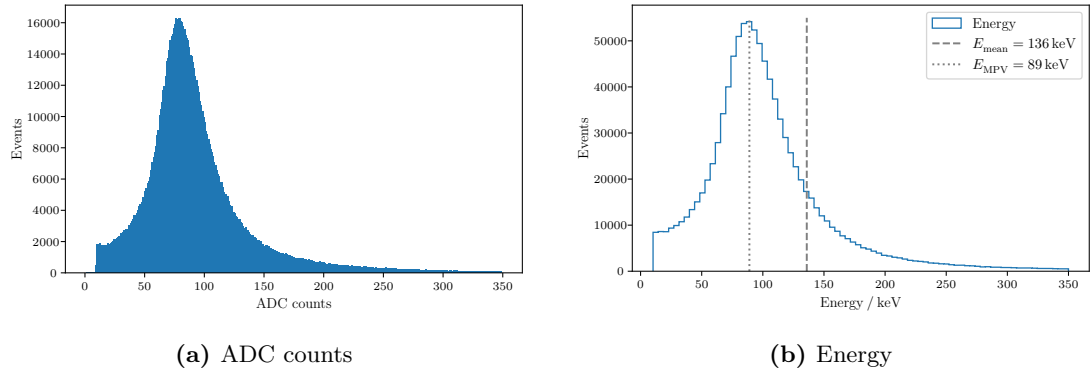


**Figure 20:** Spreading of the ADC counts and energy.

## 5 Discussion

As mentioned in section 4, the experimental setup malfunctioned during data taking. Only the data for the current-voltage characteristic was taken. The data for the other tasks was provided. However, since the detector unit was malfunctioning after, it is questionable if the data taken for the first task is fully trustworthy. Also, since the other data was provided from another experimental group, it cannot be confirmed, that the data was taken correctly. So all of the results are to be taken with caution.

For the current-voltage characteristic, a depletion voltage of 60 V was determined. According to the informational sheet given, the depletion voltage should be somewhere around 60 - 70 V [4]. The depletion voltage cannot be obtained with full confidence, since the obtained current-voltage characteristic seems inaccurate. A clear kink should be visible in the obtained data. However, only a slight curvature is visible. This might as well result from the apparatus malfunctioning and giving inaccurate data.

As for the pedestal and noise measurement, the results seem valid. The common mode shift follows a gaussian distribution as expected and the noise follows an approximate uniform distribution as it would be expected from noise.

The calibration measurements on the one hand show, that all tested channels yielded the same results and they also give a clear ADC counts - charge - relation. A polynomial function was fitted to the data and resulted in a function, that can be used for the other tasks.

By shifting the location of the laser, the pitch and width can be extracted. The resulting widths are  $d_{\text{strip}} = 100 \mu\text{m}$  and the pitch is  $p_{83} = 120 \mu\text{m}$  for channel 83 and  $p_{84} = 110 \mu\text{m}$  for channel 84. The values are approximate values extracted visually from the graphical representation of the data. Therefore, no exact deviation would make sense and although the pitches of the two channels differ, they are compliant with each other if one regards the approximation.

The charge collection efficiency was calculated for the laser and for the source measurement. The penetration depth resulting from a fit of the data to Equation 10 is determined as 980 nm. Literature values for the penetration depth of a laser with a wavelength of 980 nm was not provided by the instructions and also not found online. However, values for a wavelength of 960 nm and 1073 nm were provided for which the penetration depth is 74  $\mu\text{m}$  and 380  $\mu\text{m}$  respectively [4]. Therefore, the results are compliant with the given literature value. As for the source scan, the resulting plot is similar to the CCE plot for the laser measurement. As expected, the counts become constant as the depletion voltage is reached. The source measurement reaffirms the laser measurement.

For the large source scan, hitmap of the distribution of the events per channel shows has a gaussian shape most likely centered around the location of the source. The calculated mean energy of  $E_{\text{mean}} = 135.94 \text{ keV}$  corresponds to an energy deposition of 4.53 MeV/cm. Comparing this value to the theoretical value for pure silicon of 3.88 MeV/cm (see 2.4.2), a deviation of 16.8 % arises. This could be explained with the doping of the silicon of the sensor, leading to a higher energy deposition. Additionally, the absorption of electrons in other matter sitting between the source and the sensor would need to be considered for more precise results. The fit function used to calculate the energy is also only valid for

low ADC counts and can therefore skew the results.

## References

- [1] *Band gap comparison*. Wikimedia Commons. URL: [https://commons.wikimedia.org/wiki/File:Band\\_gap\\_comparison.svg](https://commons.wikimedia.org/wiki/File:Band_gap_comparison.svg) (visited on 11/05/2024).
- [2] Thomas Corona. ‘Simulation Tools for the 2KM detector at the T2K Experiment’. In: ().
- [3] W .R. Leo. *Techniques for nuclear and particle physics experiments*. Jan. 1987. URL: <https://www.osti.gov/biblio/5711102>.
- [4] *V15 - Characerization of silicon strip sensors*. TU Dortmund, Faculty of Physics. 2024. URL: [https://moodle.tu-dortmund.de/pluginfile.php/2306060/mod\\_resource/content/2/Anleitung\\_Studenten\\_Hannah-EN.pdf](https://moodle.tu-dortmund.de/pluginfile.php/2306060/mod_resource/content/2/Anleitung_Studenten_Hannah-EN.pdf).
- [5] Pauli Virtanen et al. ‘SciPy 1.0: Fundamental Algorithms for Scientific Computing in Python’. In: *Nature Methods* 17 (2020), pp. 261–272. DOI: 10.1038/s41592-019-0686-2.